Ocean Engineering 286 (2023) 115598

Contents lists available at ScienceDirect

Ocean Engineering

journal homepage: www.elsevier.com/locate/oceaneng

Hydraulic performance analysis for homogeneous mound breakwaters: Application of dimensional analysis and a new experimental technique

Pilar Díaz-Carrasco

Department of Transportation, ETSI Caminos, Universitat Politècnica de València, 46022, Valencia, Spain

ARTICLE INFO

Keywords:
Mound breakwaters
Laboratory technique
Wave energy transformation
Wave-breaking
Porous media
Relative water depth
Wave steepness

ABSTRACT

The main objective of this study is to apply the methodology proposed by Díaz-Carrasco et al. (2020), based on the dimensional analysis and a new experimental technique, to estimate and study the wave energy transformation on homogeneous mound breakwaters. The dimensional analysis includes the main variables of wave train, porous media and slope geometry that influence the hydraulic performance on mound breakwaters. For that, laboratory tests were performed in a wave flume for a homogeneous and permeable mound breakwater. A new experimental technique derived from the methodology of Díaz-Carrasco et al. (2020) is also applied for designing wave conditions in laboratory based on the interplay that the relative water depth, h/L, and the wave steepness, H/L, has on the hydraulic performance of the structure, called the sample space. An analysis was conducted to study the influence that each dimensionless variable has on wave energy transformation. The experimental results shows that there is a relationship between the reflected, K_R^2, transmitted, K_T^2, and dissipated energy, D^*, and the product of the relative water depth, h/L, and the incident wave steepness, H_I/L. The selection of wave conditions from the new experimental technique of sample space allows quantifying regions of wave energy transformation and wave breaker types on the breakwater and it seems to be a useful technique for designing laboratory conditions.

1. Introduction

Rubble mound breakwater is the most frequent breakwater typology in the world due to its ability to dissipate the wave energy, its relatively simple design and the possibility to be constructed using pieces of different types and sizes. Within this typology, use of homogeneous and permeable mound breakwaters without multi-layer cross sections has seen a pronounced expansion in coastal engineering. Most of these structures are built to protect navigation channels and harbours, but they are also considered for using in beach stabilisation and shore protection (Ahrens, 1984, 1989). In general, the latter applications are possible thanks to the advantages offered by this mound typology compared to others, such as: (1) its high porosity makes it more stable than a rubble mound breakwater with main armour layer, (2) it dissipates energy effectively and, (3) its design simplicity and low environment impact are significant factors in keeping down constructions costs and being an optimum structure and a natural-based solution in many situations (Odériz et al., 2018; Molines et al., 2021).

The design project, construction and maintenance of mound breakwaters must be verified to provide safety and service in coastal areas during its useful life. The performance of these coastal structures depends on the kinematic and dynamic regimes and its quantification should consider the three laws of (1) energy conservation, used to estimate the energy transformation in wave-structure interaction; (2) mass conservation, applicable to estimate run-up, run-down and overtopping; and (3) momentum conservation, used to calculate the forces and momentums on the pieces that form the structure (stability analysis). In order to design stability and overtopping formulas for these coastal structures, their hydraulic performance should first be analysed, which includes the phenomena of wave progression and energy transformation (reflected, K_R^2, transmitted, K_T^2, dissipated energy, D^*) on the slope.

Most of the formulas used for quantifying the hydraulic performance on mound breakwaters are based on the seminal work of Battjes (1974), who proposed using Iribarren number, ξ, (Iribarren and Nogales, 1949) as the dynamic similarity parameter to analyse wave energy transformation on breakwaters and to identify wave breaker types over the slope. Since then, most of the design formulas are combinations of Iribarren number with both dimensionless and dimension variables selected on empirical grounds rather than on dimensional analysis. Díaz-Carrasco et al. (2020), Moragues and Losada (2021), Díaz-Carrasco et al. (2021), Losada (2021) demonstrated that there is a high scatter of the wave energy formulas, breaker types, overtopping and stability formulas, as the Iribarren number increases. These current

E-mail address: pdiacar@upv.es.

https://doi.org/10.1016/j.oceaneng.2023.115598
Received 10 January 2023; Received in revised form 28 July 2023; Accepted 10 August 2023
Available online 20 August 2023

Nomenclature

Symbol	Description
B_b	Crown width
B_{eq}	Characteristic width (Kortenhaus and Oumeraci, 1998)
B^*	Base width
D^*	Bulk dissipation energy
$D_{n50,a}$	Armour diameter
$D_{n50,p}$	Core diameter
F_{MT}	Height of the breakwater
F_c	Free-board
g	Gravity acceleration
h	Water depth
H	Wave height
H_I	Incident wave height
K_R	Wave reflection coefficient
K_T	Wave transmission coefficient
L	Wavelength obtained by the wave period T and linear dispersion
n_p	Core porosity
$R_{e,Da}$	Armour Reynolds number
$R_{e,p}$	Core Reynolds number
T	Wave period
U	$\approx n_p H/T$ Characteristic seepage velocity
α	Seaward slope angle
β	Landward slope angle
χ	Similarity parameter defined by Díaz-Carrasco et al. (2020)
ν	Kinematic water viscosity
ρ_s	Rock/Cube unit density
ξ	$= \tan(\alpha)/\sqrt{(H/L)}$ Iribarren number

experimental formulas are derived from an extensive experimental database and fitted by calibrating coefficients and including/mixing variables without prior analysis of the parameters that influence the design variable. In addition, the formulas obtained are derived from experiments tested with very specific test conditions, experimental devices and techniques. The consequences of these analyses and methods result in a high epistemic uncertainty of the results and thus of the developed formulas. This uncertainty seems unacceptable not only because of the knowledge and means available, but also because of the future challenges resulting from sea level rise that will require greater precision and optimisation (economically and environmentally) in design.

Consequently, the main objective of this study is to apply a specific methodology developed in recent years by Díaz-Carrasco et al. (2020) in order to estimates and study the energy transformation of incident waves that interact with a homogeneous mound breakwater. The methodology is based on dimensional analysis which includes the main variables of wave train, porous media and slope geometry that influence the hydraulic performance of slope breakwaters. A new experimental technique derived from the methodology of Díaz-Carrasco et al. (2020) is also applied for designing laboratory tests based on the interplay that the relative water depth, h/L, and the wave steepness, H/L, has on the hydraulic performance of the structure. This study involves physical laboratory experimentation in a 2D wave flume of a non-overtoppable, homogeneous and permeable mound breakwater. The structure of the paper is organised as follows: Section 2 gathers a background of the dimensional analysis and main results of Díaz-Carrasco et al. (2020). Section 3 outlines the physical tests, experimental technique and processing methods performed in IISTA-University of Granada. Section 4 presents the results of wave energy transformation and breaker types according to the variables involved in the dimensional analysis. The discussion of the experimental technique and results is gathered in Section 5. Conclusions are presented in Section 6. Finally, Appendix A details the application of the new experimental technique for selecting wave conditions in laboratory.

2. Background of wave-structure interaction analysis

Díaz-Carrasco et al. (2020) studied the wave energy transformation for an impermeable slope breakwater and a permeable slope breakwater with main armour layer on the basis of numerical and experimental tests, respectively. From these experiments, rough slope and smooth slope, Díaz-Carrasco et al. (2020) included the main geometrical and wave parameters involved in both breakwater typologies and developed a dimensional analysis (described in detail in their study) which states that the wave energy reflected (K_R^2), transmitted (K_T^2) and dissipated (D^*) are derived quantities of:

$$[K_R^2, K_T^2, D^*] = f\left(\Pi_1, \Pi_2, \Pi_3\right) \tag{1}$$

where $\Pi_1 = (h/L, H_I/L)$ represents the incident wave train that includes the relative water depth, h/L, and the wave steepness at the toe of the slope, H_I/L. $\Pi_2 = (B^*/L, D_{n50,p}/L, R_{e,p})$ gathers the influence of the porous media with: the relative base width, B^*/L, that indicates the tendency to reach the saturation regime of the structure (Requejo et al., 2002); the relative core diameter, $D_{n50,p}/L$, that governs the flow dissipation inside the porous media and quantifies the scale effects (Pérez-Romero et al., 2009); and the grain Reynolds number, $R_{e,p} = D_{n50,p}U/\nu$ (Gu and Wang, 1991; Van Gent, 1995; Burcharth and Andersen, 1995), being $U \approx n_p H/T$ the characteristic seepage velocity in the porous media. $\Pi_3 = (D_{n50,a}/L, R_{e,Da})$, includes the influence of the main armour layer with: the relative main armour diameter, $D_{n50,a}/L$, that governs the turbulence flow on the slope due to the wave-breaking and interaction with the armour layer (Clavero et al., 2018); and the armour Reynolds number, $R_{e,Da} \approx \sqrt{gH_I}D_{n50,a}/\nu$ (Dai and Kamer, 1969). The slope angle, α, is not included in Eq. (1) since it is already a dimensionless parameter that characterises the structure and orders the results.

From the dimensional analysis and the experimental results, Díaz-Carrasco et al. (2020) pointed out the following conclusions,

1. The regions of wave energy transformation and their related breaker types are the following: (i) dissipated region with spilling and weak plunging breakers; (ii) reflected region with surging breakers; and (iii) transition region, with strong plunging, strong bore and weak bore breakers. Díaz-Carrasco et al. (2020)'s study includes the variants of breaker types referred to weak/strong plunging (Lakehal and Liovic, 2011) and weak/strong bore (Zhang and Liu, 2008).
2. There is a relationship between the product $(h/L)(H_I/L)$ and the reflected, transmitted and dissipated energy on slope breakwaters. This product is defined as the similarity parameter $\chi = (h/L)(H_I/L)$, which delimits the wave energy transformation regions (reflected, dissipated and transition regions) and the wave trains with the same breaker type (Moragues and Losada, 2021).
3. The sample space defined by [$\log(h/L)$ vertical-axis, $\log(H/L)$ horizontal-axis] provides a functional relationship between water depth, h, wave height, H, and wave period, T. This functional relationship would allow designing experimental conditions in laboratory in order to characterise the regions of wave energy transformation and wave breaker types on mound breakwaters.

The main results of Díaz-Carrasco et al. (2020) suggest applying this analysis methodology to more laboratory tests in order to verify the correct study of wave-structure interaction.

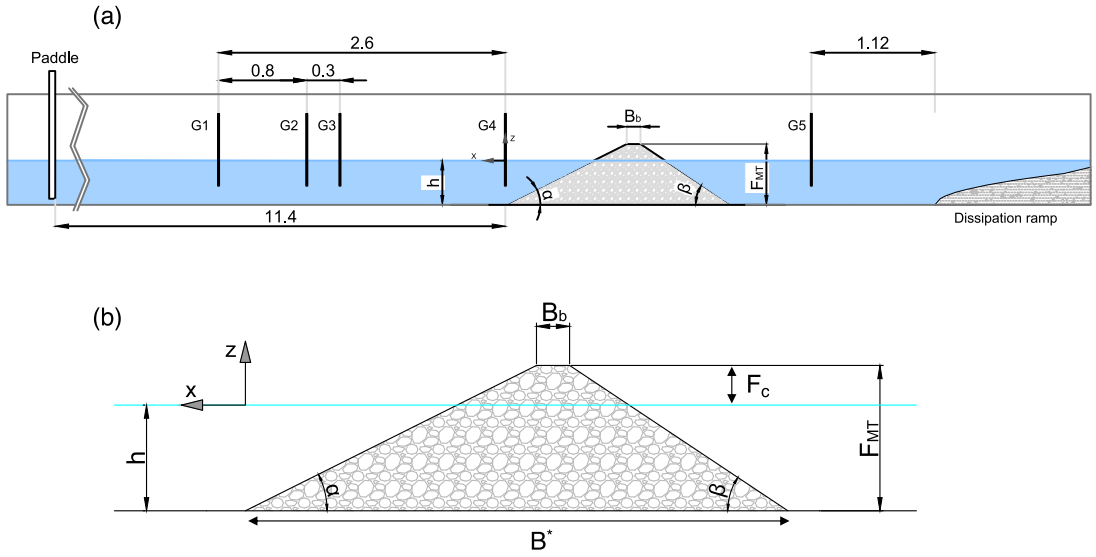

Fig. 1. (a) Diagram of the wave flume and location of wave gauges (dimensions in metres), (b) physical model of the homogeneous and permeable mound breakwater tested (HP-MB).

Table 1
Geometric parameters of the physical models tested. B_b is the crown width of the breakwater; B^* is the base width of the breakwater; and α and β are the seaward and landward slopes of the breakwater, respectively.

Configuration	B_b (m)	tan(α)	tan(β)	B^* (m)
HP-MB-1	0.24	1/2	1/1.5	2.165
HP-MB-2	0.24	1/1.5	1/1.5	1.890
HP-MB-3	0.10	1/2	1/1.5	2.025

3. Experimental setup

3.1. Physical tests

Experimental tests were performed in the wave flume of the Andalusian Inter-University Institute for Earth System Research (IISTA) at the University of Granada (Fig. 1a). Fig. 1b shows a diagram of the physical model tested, namely, a homogeneous and permeable mound breakwater with a constant granular diameter, $D_{n50,p}$ = 30 mm. Two different widths of the top, B_b, and two seaward slope angles, α, were tested. The water depth in the wave generation zone and in the flume was kept constant and equal to $h = 0.4$ m.

Table 1 summarises the geometrical configuration of the three physical models tested, identified hereinafter as: HP-MB-1, for $B_b = 0.24$ m, slope $\cot(\alpha) = 2$; HP-MB-2, for $B_b = 0.24$ m, slope $\cot(\alpha) = 1.5$; and HP-MB-3, for $B_b = 0.10$ m, slope $\cot(\alpha) = 2$. All the models have a constant free-board, $F_c = 0.15$ m and a breakwater height, $F_{MT} = 0.55$ m. The characteristic of the permeable and homogeneous rocks were: diameter $D_{n50,p}$ = 30 mm, density ρ_s = 2.64 tn/m^3, and porosity n_p = 0.462 according to CIRIA, CUR, CETMEF (2007).

3.2. New experimental technique: the sample space

The application of new experimental technique proposed by Díaz-Carrasco et al. (2020), called the sample space [log(h/L), log(H/L)], seeks to (i) optimise the number of experiments, (ii) verify the design criteria between model-prototype, and (iii) quantify the regions of wave energy transformation and wave breaker types. Fig. 2 shows the flow-chart of the sample space to select the wave conditions in laboratory according to experimental requirements. The wave conditions of wave height, H, and wave period, T (or wavelength, L by dispersion equation $f(h,T)$), for a given water depth, h, can be selected as follow:

- *Step 1:* According to the experimental requirements, such as experimental tests under non-overtopping (E1), non-damage (E2) and non-breaking wave conditions (E3), the wave height could be limited to a maximum value, H_{max} and $H/h < 0.78$. The wave generation regime (E3) should be also considered as well as the limitations of the laboratory's paddle generation (E5).
- *Step 2:* Depending on the breakwater typology and considering values of previous studies and constructed maritime works of this typology, it is possible to select wave conditions of H and T that achieve the maximum reflected (R) and dissipated (D) wave energy. Points R and D close the formed parallelepiped in which h/L and H/L conditions are selected.
- *Step 3:* Selecting h/L and H/L conditions to cover the transitions of wave breaker types, such as weak/strong bore and weak/strong plunging.

This section summarises the wave conditions obtained from the application of the flow-chart of Fig. 2 to the mound breakwaters and experiments of this study. Appendix A describes in detail the direct application of the sample space for the laboratory tests of this study.

The experimental tests were performed with the following requirements:

1. Wave-breaking was only caused by wave-breakwater interaction and the experiments were also under non-overtopping and non-damage conditions.
2. The AwaSys software package was used to generate waves with the simultaneously active absorption of reflected waves. The IISTA paddle generation system was limited by: $H > 0.02$ m and $T > 1$ s.
3. Regular waves in Stoke I regime were simulated and defined by a wave height, H, and a wave period, T. Each test was repeated three times with 100 of waves per test.

Regular wave conditions of H and T (target conditions) were selected by complying with the functional relationship of the sample space [log(h/L), log(H/L)] to cover the regions of wave energy transformation and breaker types. Note that throughout this study when the wave height is identified by H or H_I it refers to the conditions of target and incident wave height (obtained by separation of the incident and reflected wave trains), respectively. Table 2 gathers the wave conditions for the three physical models tested. For further information on the application of this experimental technique see Appendix A.

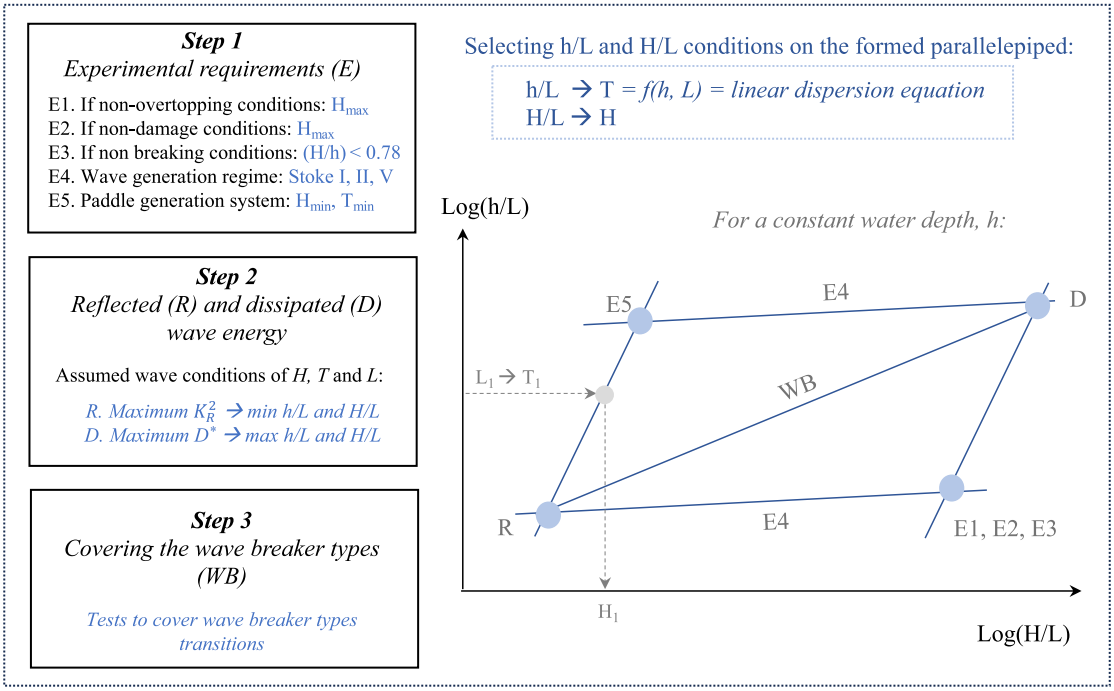

Fig. 2. Flow-chart of the new experimental technique proposed by Díaz-Carrasco et al. (2020), called sample space, to select the wave conditions in laboratory according to the experimental requirements.

Table 2
Minimum and maximum values of waves conditions tested in laboratory (H, T) following the sample space [$\log(h/L)$, $\log(H_I/L)$] described in Appendix A.

Wave parameter	Range
T (s)	[1.020–3.640]
H (m)	[0.021–0.121]
h/L	[0.060–0.280]
H/L	[0.005–0.026]

3.3. Wave measurements and data processing

The experimental incident and reflected wave trains were separated using the method suggested by Baquerizo (1995), which gives the magnitude and phase of the reflected wave train. The reflected and transmitted wave energy, E_R, E_T, and their respective reflection (K_R^2 and phase ϕ_R) and transmission coefficients (K_T^2) were obtained by applying power spectral analysis. K_R^2 and ϕ_R were calculated with the data measured by gauges G1, G2 and G3 (see Fig. 1a). The transmission coefficient (K_T^2) was computed with the data measured with gauge G5. Gauge G4, located at the toe of the structure (x = 0), provided the total wave height at the toe of the breakwater (due to the interaction of the incident and reflected wave trains). The total bulk dissipation per unit of wave incident energy, D^*, is determined by solving the wave energy conservation equation

$$K_R^2 + K_T^2 + D^* = 1 \tag{2}$$

The statistical parameters of incident wave height, H_I, wave period, T, and wavelength, L, were obtained from the temporal analysis of the time series. For each regular test, wave breakers on breakwater slope were identified by photographs and test recording; thus, surging, weak/strong bore and weak/strong plunging breakers were identified.

4. Analysis of wave-structure interaction results

This section analyses the results of wave energy transformation [K_R^2, K_T^2, D^*] for the homogeneous and permeable mound breakwaters tested by the following steps: first, the hydraulic performance of the permeable breakwater (rough slope) is compared with the numerical results obtained in the IH-2VOF model (Lara et al., 2008a) of an impermeable breakwater (smooth slope) with the same slope and water depth condition (see Appendix B for further details of the numerical tests); then, the influence on wave energy transformation of the dimensionless parameters representing the incident wave train, the porous media, and the slope angle, is analysed.

4.1. Hydraulic performance of a permeable slope versus an impermeable slope

Figs. 3a and 3b show the sample spaces [$\log(h/L)$, $\log(H_I/L)$] for the impermeable breakwater modelled numerically in IH-2VOF by Díaz-Carrasco et al. (2020) and the homogeneous and permeable HP-MB-1 model tested in this study, respectively. For both breakwaters the water depth was constant, $h = 0.4$ m, and the slope angle $\cot(\alpha) = 2$. Wave breaker types are identified by colour-bands for the impermeable slope and by colours for the permeable HP-MB-1 slope. The isolines of constant values of $\chi = (h/L)(H_I/L)$ are also marked. It is observed that in both sample spaces the density of the results is similar in the range $0.001 \leq \chi \leq 0.0065$. This region corresponds to wave heights and wave periods normally tested both in laboratory and numerically. For the permeable slope, whose wave conditions (H and T) comes from the experimental technique detailed in Appendix A, this range $0.001 \leq \chi \leq 0.0065$ encompasses the zones selected to cover the transitions of wave breaker types (weak/strong bore and weak/strong plunging). Comparing both sample spaces it is observed that, for the same slope $\cot(\alpha) = 2$ and $h = 0.4$ m, the breaker types for the homogeneous and permeable HP-MB-1 breakwater are shifted to lower values of χ with respect to the impermeable one. For instance, the same breaker type, strong plunging, occurs with lower values of wave steepness H_I/L and relative depth h/L in the permeable slope case. The presence of a porous media, in particular the flow within it, changes and determines the phase lag between the incident and reflected wave trains and this impacts on the wave breaker type. For the same relative water depth and wave steepness, wave-breaking will tend to be more dissipative breaker type on a permeable slope than on an impermeable slope.

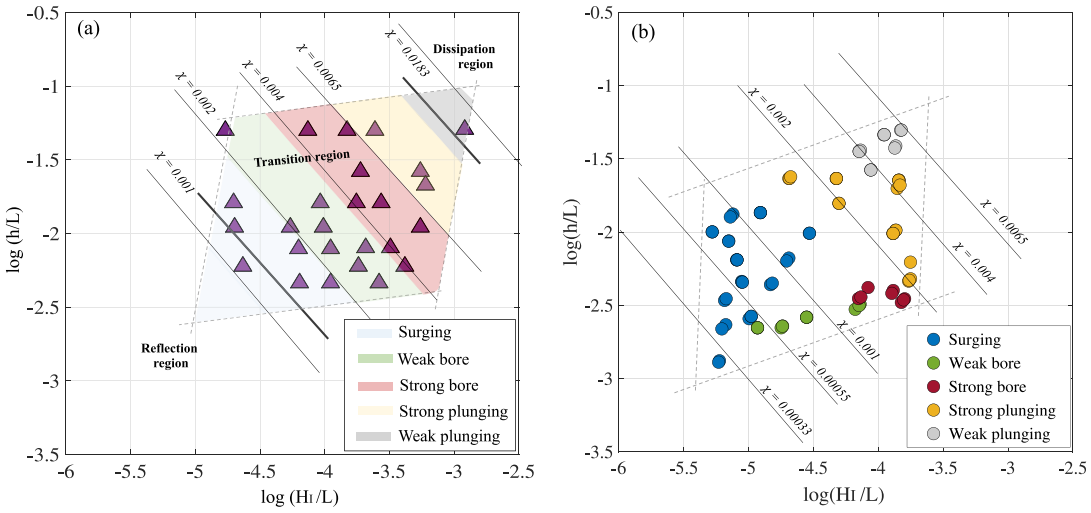

Fig. 3. Sample spaces $[\log(h/L), \log(H_I/L)]$ for (a) an impermeable slope breakwater with slope $\cot(\alpha) = 2$ modelled by Díaz-Carrasco et al. (2020), and (b) the homogeneous and permeable slope HP-MB-1 tested in laboratory with slope $\cot(\alpha) = 2$. Black line represents the isolines with constant values χ. Colours are used to identify the breaker types.

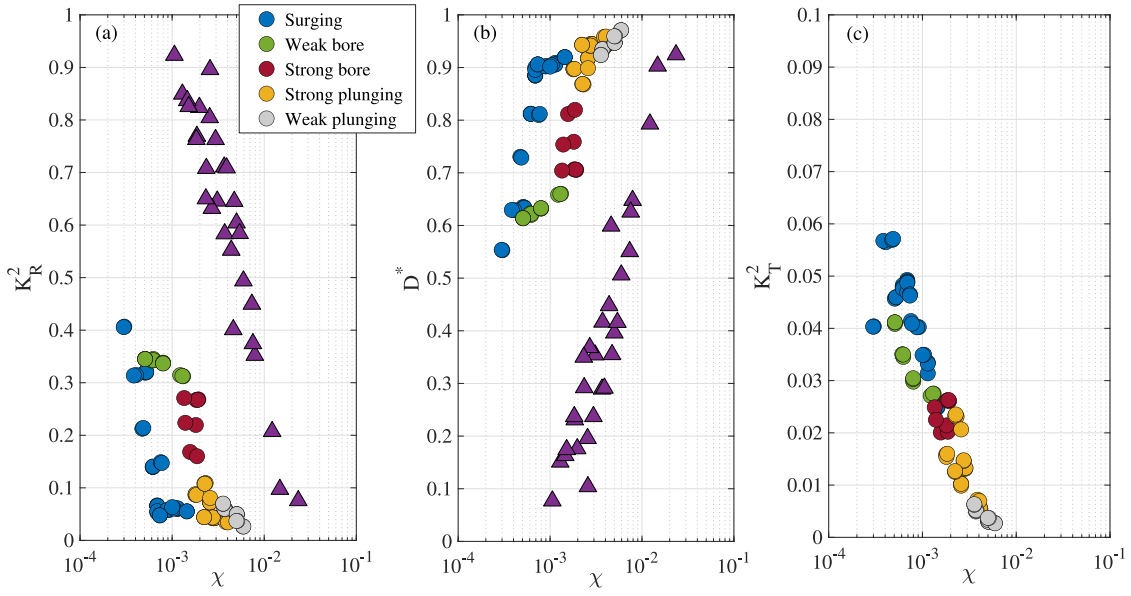

Fig. 4. Wave energy transformation against the product of the wave steepness and the relative water depth, $\chi = (h/L)(H_I/L)$: (a) reflected energy coefficient K_R^2, (b) bulk wave dissipation D^*, and (c) transmitted energy coefficient K_T^2. Circles-symbols are the experimental results of the homogeneous and permeable slope HP-MB-1 tested with slope $\cot(\alpha) = 2$ and $B^* = 2.165$ m, and triangle-symbols are the numerical results of the impermeable slope $\cot(\alpha) = 2$ modelled by Díaz-Carrasco et al. (2020). The breaker types of the experimental results are identified by colours.

Fig. 4 represents the results of wave energy transformation coefficients against the similarity parameter $\chi = (h/L)(H_I/L)$, for the same data represented in Fig. 3: (circles) homogeneous and permeable HP-MB-1 model with slope $\cot(\alpha) = 2$, (triangles) impermeable slope $\cot(\alpha) = 2$ of Díaz-Carrasco et al. (2020). Despite having the same slope angle, the results for the permeable slope are shifted to lower values of χ. For the same value of χ, the permeable breakwater reflects much less energy with more dissipated breaker types (Fig. 3) than the impermeable structure. Fig. 4 also shows that for small variations in χ, with $\chi > 10^{-3}$, different wave breaker types are observed in laboratory, from weak bore to weak plunging with increasing χ, and large variations in K_R^2, D^* and K_T^2 occur. A remarkable feature in the experimental results is the presence of a data set for the surging and weak bore breaker types, leading to different K_R^2 values for the same χ value depending on the breaker type (e.g. $\chi = 0.001$). Coincidentally, the highest K_T^2 values occur in this data set (hereinafter referred to as singularity). In the impermeable slope, for the same value of χ, for example $\chi = 0.002$, it is observed some dispersion in K_R^2 results but the wave breaker types are ordered according to χ values as it is shown in Fig. 3a. Specifically, in the interval $0.002 \leq \chi \leq 0.0065$, it is observed weak bore, strong bore and strong plunging breaker types, which generate a dispersion in wave energy transformation (Díaz-Carrasco et al., 2020).

The comparison of permeable results to those of the impermeable breakwater with the same slope angle highlighted significant changes in the performance of the permeable breakwater. The different behaviour of the permeable breakwater compared with the impermeable one is due to the role that the porous media and its interaction with the incident wave train $(h/L,\ H_I/L)$ has in the hydraulic performance of the homogeneous and permeable structure. As pointed out in Díaz-Carrasco et al. (2020), for a homogeneous and permeable breakwater the wave energy transformation (K_R^2, K_T^2 and D^*) and wave breaker types also depend on the relative width, B^*/L, the relative core diameter, $D_{n50,p}/L$, and the grain Reynolds number, R_{ep}.

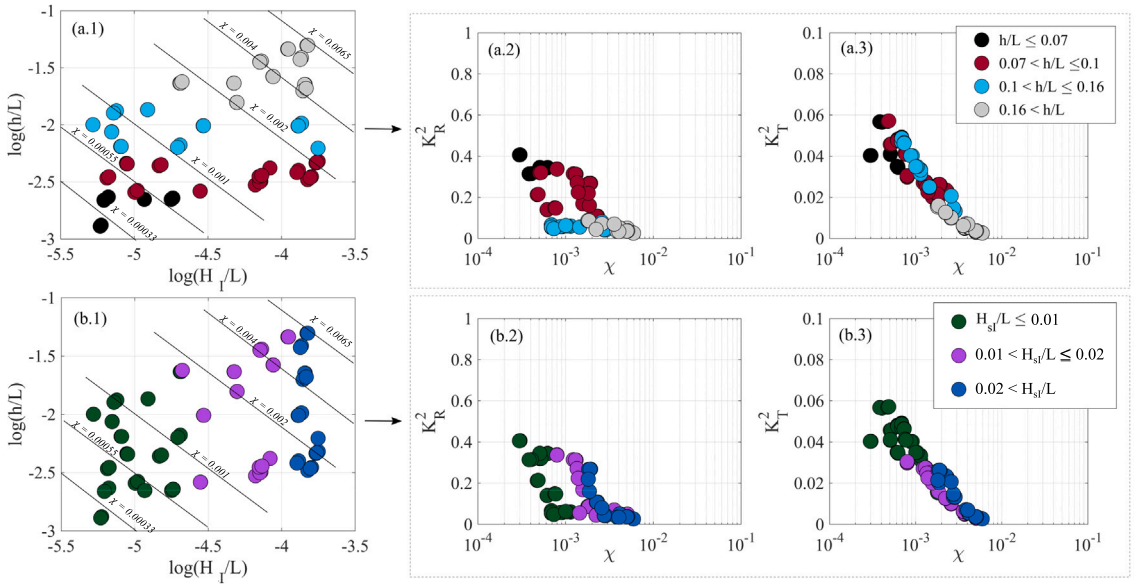

Fig. 5. Analysis of the incident wave train characterised by: (a) the relative water depth, h/L, and (b) the wave steepness, H_I/L. Figs (a.1) and (b.1) are the sample spaces coloured by ranges of h/L and H_I/L, respectively. Figs. (a.2, a.3) and Figs. (b.2, b.3) represent the reflected energy coefficient, K_R^2, and transmitted energy coefficient, K_T^2, against χ coloured by ranges of h/L and H_I/L, respectively. The experimental results are for the homogeneous and permeable HP-MB-1 model with slope $\cot(\alpha) = 2$ and base width $B^* = 2.165$ m.

4.2. Influence of dimensionless parameters on hydraulic performance

This section analyses the influence of the dimensionless parameters presented in Eq. (1) for a homogeneous and permeable breakwater (Π_1, Π_2 in Eq. (1)), which are not constant in the experimental tests, and the slope angle, α. In the following the experimental results of dissipation, D^*, are not represented since its values follow a opposite trend to the reflection coefficient (K_R^2), because of the low values of transmission coefficients ($K_T^2 < 0.06$).

4.2.1. Incident wave train

Fig. 5 represents the influence of the incident wave train, h/L and H_I/L, on the experimental results for the homogeneous and permeable HP-MB-1 model with slope $\cot(\alpha) = 2$ and base width $B^* = 2.165$ m. Figs. 5a.1 and 5b.1 locate the ranges of values of h/L and H_I/L in the sample space and its relation with the regions of wave energy transformation and breaker types. For the lower values of relative water depth, $h/L \leq 0.07$, the maximum reflection of the structure occurs (Fig. 5a.2) and surging/weak bore breaker types are observed (see Figs. 3b and 4). As h/L increases and for wave steepness $H_I/L > 0.01$ (Fig. 5b), the wave breaker types progress from weak bore to weak plunging, and the reflection of the breakwater decreases (see Figs. 5a.2 and 5b.2, respectively). For wave energy transmitted, small changes in h/L do not result in large changes in K_T^2.

For each range of wave steepness H_I/L defined – $H_I/L \leq 0.01$, $0.01 < H_I/L \leq 0.02$, $0.02 < H_I/L$ – Fig. 5b.2 shows that the reflection coefficient is larger ($K_R^2 > 0.3$) or smaller ($K_R^2 < 0.1$) depending on whether h/L value is high or low, respectively (Fig. 5a.2). As H_I/L increases, K_T^2 decreases (Fig. 5b.3) and breaker types progress from surging to weak plunging (Figs. 3b and 4). For the experimental data with $H_I/L \leq 0.01$, the transmitted coefficient takes the highest values (maximum $K_T^2 = 0.057$) and the breaker types observed are surging and weak bore. These values of $H_I/L \leq 0.01$ are in the singularity mentioned in Fig. 4.

Fig. 5 shows that as χ increase, K_R^2 and K_T^2 decrease except at the singularity mentioned above with values of $H_I/L \leq 0.01$. It seems that the results of wave reflection and transmission depend more on the relative water depth and on the wave steepness, respectively: K_R^2 decreases as h/L increases and K_T^2 decreases as H_I/L increases. Wave breaker types are ordered according to increasing values of χ, from surging to weak plunging. The breaker type conditions the amount of reflected, dissipated and transmitted energy. For a constant water depth, h, as the wave period decreases and wave height increases, the incident wave train becomes more unstable and tend to dissipate more energy when it interacts with the structure. The more energy dissipated (lower K_R^2), the lower flow through the porous media and therefore lower values of K_T^2.

4.2.2. Geometric configuration of the porous media

Fig. 6 represents the sample space and the experimental values of K_R^2 and K_T^2 against χ, coloured by ranges of B^*/L, for the two physical models tested with different size of porous media: (circles) HP-MB-1 model with top width $B_b = 0.24$ m and base width $B^* = 2.165$ m, (squares) HP-MB-3 model with top width $B_b = 0.10$ m and base width $B^* = 2.025$ m. For both models, the slope angle is $\cot(\alpha) = 2$ and the diameter of the porous media is $D_{n50,p} = 30$ mm. Fig. 6a locates the ranges of values of B^*/L in the sample space and its relation with the regions of wave energy transformation and breaker types. Fig. 6 shows that the range of values of B^*/L are grouped in the same intervals of χ for both models with different porous media area. The reflected energy of the breakwater, K_R^2, increases (D^* decreases) as B^*/L decreases (Fig. 6b). For large relative width, $B^*/L > 3/4$ or $B_{eq}/L > 0.25$ (being B_{eq} a characteristic width of the porous media (Kortenhaus and Oumeraci, 1998)), the reflection coefficient achieves a minimum and constant value. In this region and for the results with $H_I/L > 0.01$ (Fig. 5), the wave energy dissipated, D^*, takes the highest values and the breaker types observed are strong/weak plunging (Fig. 4). The transmitted energy, K_T^2, takes maximum and minimum values with the lowest and highest range of B^*/L, respectively (Fig. 6c). The trend is that K_T^2 decreases as B^*/L increases although it is not as evident as in K_R^2 results. In intermediate B^*/L ranges, K_T^2 results depends more on the wave steepness and the wave breaker type.

Fig. 6 shows that the results of K_R^2 and K_T^2 for range of B^*/L have the same trend as for h/L ranges (Fig. 5a.2). The relative width of the breakwater, B^*/L, marks the saturation regime of the structure in laboratory, that is, when the breakwater cannot reflect and transmit (throw the porous media) more energy, and it reaches a constant minimum value of K_R^2. For the results with $H_I/L > 0.01$, the saturation

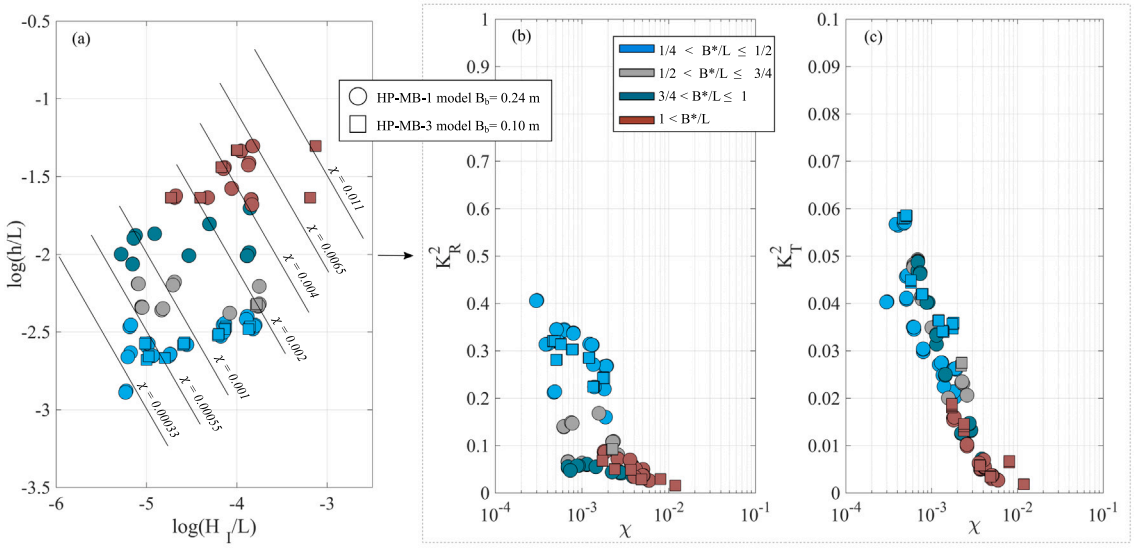

Fig. 6. Analysis of the porous media characterised by the relative base width B^*/L, whose ranges are identified by colours: (a) sample spaces with the isolines of χ constant marked (black-lines); (b) and (c) the reflected energy coefficient, K_R^2, and transmitted energy coefficient, K_T^2, against χ, respectively. The experimental results are for the homogeneous and permeable models: (circles-symbols) HP-MB-1 model slope $\cot(\alpha) = 2$ and base width $B_b = 0.24$ m, (squares-symbols) HP-MB-3 model slope $\cot(\alpha) = 2$ and base width $B_b = 0.10$ m.

regime is achieved at $\chi \approx 0.002$ for range of $B^*/L > 1$, with minimum values of K_R^2 and K_T^2. In the singularity mentioned with $H_I/L \leq 0.01$, there are minimum values of K_R^2 with $3/4 < B^*/L < 1$ but these values do not correspond to a saturation regime since K_T^2 takes high values; the origin of this singularity will be explained below.

4.2.3. Seaward slope angle

Fig. 7 shows the influence of the seaward slope angle, α, in the hydraulic performance of the structure. Wave breaker types are identified by colours. The experimental results show that K_R^2 results are ordered by the slope angle. In fact, there is a slight displacement along the x-axis to higher values of χ for the experimental data with slope $\cot(\alpha) = 1.5$. This displacement is also reflected in the sample space shown in Fig. 7a. For the same value of χ and breaker type, e.g. $\chi = 0.002$ and weak bore breaker, the slope $\cot(\alpha) = 1.5$ tends to reflect more energy (dissipate less) than the slope $\cot(\alpha) = 2$ (Fig. 7b). In this case, the transmitted energy for $\chi = 0.002$ and weak bore breaker is practically the same for both slope angles (Fig. 7c). Except for the singularity data mentioned, Fig. 7 also shows that wave breaker types are ordered by values of χ, from weak bore to weak plunging as χ increases, for each slope angle tested.

Although the differences between the two slopes angles are not significant because the tested slopes are very close to each other, Fig. 7 shows that as the slope angle increases, the breakwater tends to reflect more energy and dissipate less. The maximum reflection would occur with a completely vertical wall. In the case of transmitted energy by flow inside the porous media, both slopes have practically the same values of K_T^2 for each value of χ and wave breaker type. Note that for $\chi > 0.002$ corresponding also to $B^*/L > 1$ (Fig. 6), both slope angles reflect the same energy since both slopes achieve the saturation regime in laboratory.

4.2.4. Flow regimes inside the porous media

Flow regimes inside the porous media for the three permeable and homogeneous tested breakwaters are gathered in Fig. 8. The flow regimes limits are established according to Burcharth and Andersen (1995) by interval of grain Reynolds number, $R_{e,p} = U D_{n50,p}/\nu$. Fig. 8a locates the ranges of values of $R_{e,p}$ in the sample space and its relation with the regions of wave energy transformation and breaker types. Results show that laminar ($R_{e,p} < 150$), transition ($150 < R_{e,p} < 300$), and turbulent ($R_{e,p} > 300$) flow regimes are present inside the porous media. It is observed that in the laminar regime, wave steepness is $H_I/L < 0.01$ (Fig. 5b) and only surging breaker types are observed (Fig. 4). In this regime, the K_R^2 decreases (dissipation increases) with increasing χ (Fig. 8b), but the K_T^2 results are maximum in this interval (Fig. 8c). For the transition regime, the values of K_R^2 are high or low (conversely D^*) for the same χ value, K_T^2 decreases with increasing χ, and surging/weak bore breakers types are observed (Fig. 4) with values of wave steepness, $H_I/L < 0.01$ and $0.01 < H_I/L < 0.02$ (Fig. 5b).

Fig. 8 shows that the singularity data mentioned above are in laminar and transition regimes, with high values of K_T^2, surging and weak bore breakers observed, and maximum and minimum K_R^2 values for the same value of χ. In the turbulent regime, K_R^2 and K_T^2 decrease with increasing χ, and the breaker types observed progress from weak bore to weak plunging with increasing χ (Fig. 5b). Hence, it seems that in the laminar and transition flow regimes the hydraulic performance of the structure with χ changes with respect to the hydraulic performance in the turbulent regime.

The flow regime inside the porous media depends also on the relative diameter of the porous media, D_{n50}/L (Pérez-Romero et al., 2009). In this experimental tests, D_{n50} is constant for the three physical models. Although the effect of D_{n50}/L cannot be analysed in this study, it seems that a lower value of D_{n50} would result in a less turbulent flow inside the porous media and thus less wave energy dissipated (Vílchez et al., 2016; Díaz-Carrasco, 2019).

5. Discussion regarding the experimental design technique

The project design of a coastal structure should address the verification in laboratory of the hydraulic performance and the failure modes that can affect the structure during its service life. These predictions are influenced by many uncertainties, generally known as intrinsic and epistemic uncertainty (Van Gelder, 2001). Epistemic uncertainty is related to current knowledge regarding processes, models, observations and methods. Intrinsic uncertainty (or statistical uncertainty) is aleatory and is derived from outcomes that cannot be predicted and are treated as scholastic. This section discusses the epistemic uncertainty associated to the experimental design technique and observations that could have conditioned the results presented in Section 4.

Laboratory experiments for mound breakwaters in a wave flume should be based on the following model-prototype similarities: (1) dynamic similarity of wave progression and energy transformation on the

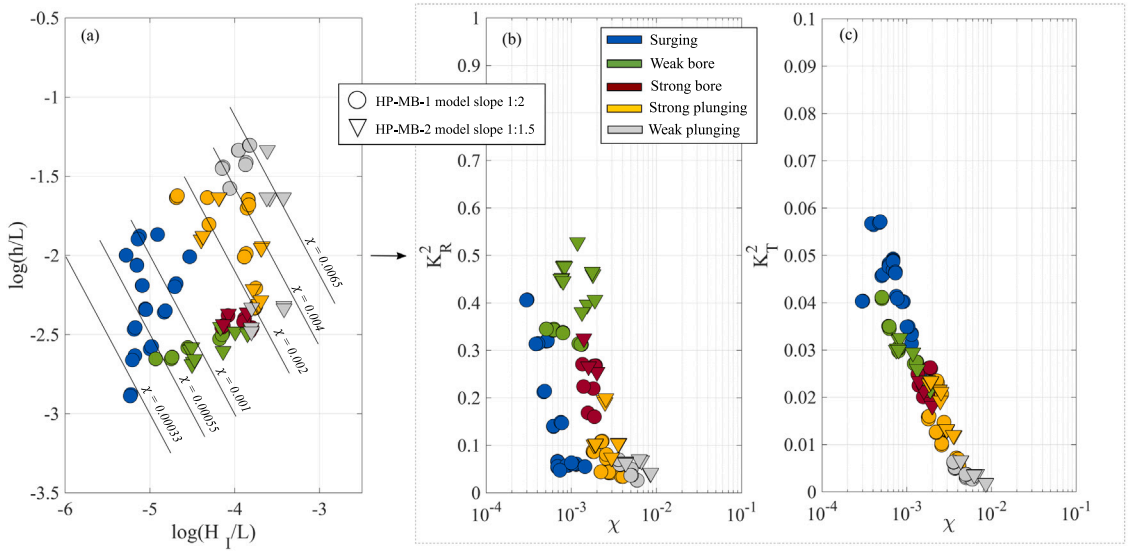

Fig. 7. Analysis of the slope angle α: (a) sample spaces with the isolines of χ constant marked (black-lines); (b) and (c) the reflected energy coefficient, K_R^2, and transmitted energy coefficient, K_T^2, against χ, respectively. The experimental results are for the homogeneous and permeable models: (circles) HP-MB-1 model slope $\cot(\alpha) = 2$, (triangles) HP-MB-2 model slope $\cot(\alpha) = 1.5$. Wave breaker types are identified by colours.

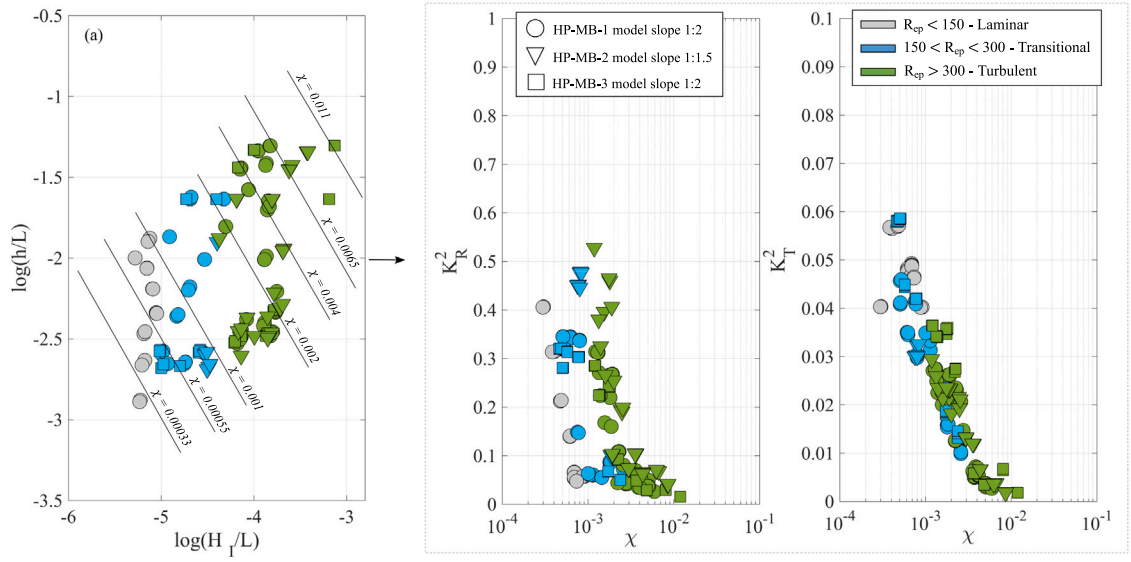

Fig. 8. Analysis of flow regimes inside the porous media. Colours delimit the flow regimes according to intervals of grain Reynolds number, $R_{e,p}$, established by Burcharth and Andersen (1995): (a) sample spaces with the isolines of χ constant marked (black-lines); (b) and (c) the reflected energy coefficient, K_R^2, and transmitted energy coefficient, K_T^2, against χ, respectively. The experimental results are for the three homogeneous and permeable models tested: (circles) HP-MB-1, (triangles) HP-MB-2, (squares) HP-MB-3.

slope; and (2) flow similarity by satisfying fully turbulent regimes in the water column and inside the porous structure. In terms of laboratory scale, Froude and Reynolds numbers cannot be kept simultaneously similar to their prototype values, so Froude scaling is used and Reynolds number is assumed to be high enough to consider a fully turbulent flow. This assumption is generally correct for the main armour layer, but it does not stand for filter layers and porous core. If the flow regime inside the porous media (core and filter) in the model differs from that inside the prototype, the hydraulic performance of the structure will be modified, known as the scale effect (Scarcella et al., 2007; Pérez-Romero et al., 2009).

In this study the dynamic similarity is satisfied using the sample space, $[\log(h/L), \log(H/L)]$ to design the wave conditions in laboratory (see Fig. 2 and Appendix A). The sample space is based on the interplay that the relative water depth, h/L, and the wave steepness, H/L, has on the hydraulic performance of the structure. The selected wave conditions H and T (target) in the sample space also depends on (i) the composition/geometry of the breakwater, (ii) the experimental conditions (e.g. non-overtopping and/or non-breaking depth-limited conditions), and (iii) the characteristic of the wave flume and its generation system. Figs. 3, 5a.1, 5b.1, 6a, 7a, 8a show the sample spaces with colours according to the dimensionless variable analysed. By comparing each sample space coloured by the dimensionless variable, it is possible to analyse the interplay that the relative water depth, h/L, and the incident wave steepness, H_I/L, has on each point tested and its role in the wave energy transformation and the breaker type on the structure. Moreover, the sample space identifies the wave conditions tested in laboratory that adequately represent the hydraulic performance of the maritime structure in prototype.

For a homogeneous and permeable breakwater, laboratory tests are more difficult to design and to interpret because of the role played by the porous media in achieving the flow similarity between model

and prototype. In this regard, the experimental results presented in Section 4 has a singularity highlighted in Figs. 4, 5, 6, 7 and 8. This singularity is characterised by low values of H_I/L, all ranges of h/L, $B^*/L < 1$, and laminar/transition flow regimes inside the porous media ($R_{e,p} < 300$). If the experimental tests of this singularity are scaled to prototype, e.g. with a 1:30 scale, the grain Reynolds number for all the experimental tests has a value of $R_{ep,prototype} > 2.5 \cdot 10^3$, which represents a turbulent regime in prototype. Therefore, the origin of the observed singularity in Section 4 is due to the difference in the flow regime between model and prototype (scale effect), which implies that the flow similarity is not fulfilled even though the dynamic similarity is fulfilled. As shown in Figures of Section 4, this scale effect changes the hydraulic performance of the structure with maximum values of K_T^2, maximum and minimum values of K_R^2 and observed breaker types mainly surging and few weak bore according to increasing values of χ. The experimental tests that suffer from scale effect do not represent the hydraulic performance of the prototype breakwater and should not be used as results to develop design formulas. By the contrary, when the flow similarity is fulfilled, wave energy transformation (reflection, transmission and dissipation) and wave breaker types are ordered and identified according to values of χ, as it is observed in Figures of Section 4 and also pointed out in Díaz-Carrasco et al. (2020). The results in turbulent regime represent the performance of the breakwater in prototype.

6. Conclusions

This study applied the methodology proposed by Díaz-Carrasco et al. (2020) to estimate and analyse the wave energy transformation on homogeneous and permeable mound breakwaters. The methodology is based on a dimensional analysis that includes the main variables of wave train, porous media and slope geometry that influence the hydraulic performance of mound breakwaters. For that, physical experimentation was performed in a 2D wave flume for a conventional homogeneous and permeable mound breakwater with two characteristic base widths, B^*, two seaward slope angles, α, and a constant core diameter, $D_{n50,p}$. Wave conditions in laboratory were selected following a new experimental technique based on the interplay that the relative water depth and the wave steepness has on the hydraulic performance of the structure, and it is called the sample space [$\log(h/L)$ vertical-axis, $\log(H/L)$ horizontal-axis] (Díaz-Carrasco et al., 2020). The following conclusions can derived from this study:

1. The analysis of the influence that each variable of the dimensional analysis has on wave energy transformation shows that there is a relationship between the reflected K_R^2, transmitted K_T^2 and dissipated D^* energy, and the product of the relative water depth, h/L, and the incident wave steepness at the toe of the slope, H_I/L. This result reinforces the findings of Díaz-Carrasco et al. (2020), which states that the dynamic similarity parameter, $\chi = (h/L)(H_I/L)$, identifies the regions of wave energy transformation and the wave breaker types.
2. A comparison of the permeable and homogeneous results obtained in laboratory to those of the impermeable breakwater tested numerically with the same slope angle highlighted significant changes in the performance of the permeable breakwater. The reflected energy decreased throughout the laboratory tests, in other words, in all the wave energy transformation and observed wave breaker types. The results of the permeable slope shifted towards lower values of χ, and the variation of K_R^2, K_T^2, D^* and wave breaker types depend on both χ and the porous media represented by B^*/L, $D_{n50,p}/L$ and $R_{e,p}$.
3. The analysis of the incident wave train shows that the wave energy reflected mainly decreases (dissipation increases) as h/L increases and the wave energy transmitted mainly decreases as H_I/L increases.
4. The analysis of the porous media shows that for both tested breakwaters with different porous media area, the wave energy transformation and wave breaker types are grouped in the same intervals of χ for the same ranges of B^*/L. The wave energy reflected decreases as B^*/L increases and the transmitted energy takes maximum and minimum values with the lowest and highest range of B^*/L. The saturation regime in laboratory is achieved for $B^*/L > 1$.
5. The slope, α, is a dimensionless parameter that characterises the structure and orders the results. As the slope angle increases, the wave energy reflected increases too and dissipated energy decreases. The transmitted energy for both tested slope angles is practically the same.
6. The wave conditions selected for the three permeable and homogeneous breakwaters together with the characteristics of their porous media result in the occurrence of the three flow regimes inside the porous media, i.e: laminar regime ($R_{ep} < 150$), transition regime ($150 < R_{ep} < 300$) and turbulent regime ($R_{ep} > 300$). In the laminar and transition flow regimes the hydraulic performance of the structure with χ changes with respect to the hydraulic performance in the turbulent regime.
7. The experimental results shows that there is a singularity characterised by lower values of H_I/L, all ranges of h/L, $B^*/L < 1$, and with laminar and transition flow regimes inside the porous media ($R_{e,p} < 300$). In this singularity, the transmitted energy is maximum and the reflected energy takes maximum and minimum values with observed surging and weak bore breakers. The different hydraulic performance of the breakwater in the singularity is due to the scale effects produced in laboratory. The results in turbulent regime represent the performance of the breakwater in prototype.

The analysis of wave energy transformation and breaker types for each dimensionless variable collected in the dimensional analysis allows identifying the behaviour of each test performed in laboratory. The application of the sample space [$\log(h/L)$, $\log(H/L)$] to get the functional relationship between h, H and T for designing wave conditions in laboratory (the new experimental technique) optimises the number of experiments and provides the information needed to (i) identify tests that meet the design criteria between model-prototype and wave generation requirements, and (ii) characterise the regions of wave energy transformation and breaker types for intervals of $\chi = (h/L)(H_I/L)$ and the breakwater performance with porous media and the slope angle. Hence, the methodology proposed by Díaz-Carrasco et al. (2020) based on dimensional analysis and the derived new experimental technique, is a useful and simple method, which not only improves the analysis of wave energy transformation and breaker types on mound breakwaters, but also allows obtaining experimental results that characterise the hydraulic performance of the breakwater in prototype. The latter will help to develop future formulas and to improve the current ones by controlling the experimental technique and the methods in laboratory.

The application of the new experimental technique and the analysis of the results of this study are conduced from experimental tests that cover some ranges of the parameters that influence the hydraulic performance of the structure. However, this study has some limitations, such as, the analysis of some dimensionless variables, different breakwater typologies and the applicability of the new experimental technique on overtopping and/or damage studies. More experimental tests with wider range of variation, such as the slope angle α, or including other parameters, such as the relative core diameter $D_{p,50}/L$, should be tested as a future work. Moreover, this study was based on laboratory tests under non-overtopping, non-damage and non-breaking by depth-limited conditions, which would have changed the wave energy transformation in its interaction with the structure. It is therefore essential to extend and study the application of this experimental technique to other maritime studies and experimental requirements.

Table 3
Wave conditions tested for the homogeneous and permeable mound breakwaters with slope $\cot(\alpha) = 2$ (HP-MB-1 and HP-MB-3 models).

Side	Wave conditions	$[(h/L)(H/L)]$	Pattern	Breaker types
A→B	T = 3.0 s, H = 0.0458 m T = 2.5 s, H = 0.121 m	[0.0005–0.0022]	T decreases H increases	Surging → Strong bore
B→C	T = 2.5 s, H = 0.121 m T = 1.02 s, H = 0.0313 m	[0.0022–0.0055]	T decreases H decreases	Strong bore → Weak plunging
C→D	T = 1.02 s, H = 0.0313 m T = 1.25 s, H = 0.0205 m	[0.0019–0.0055]	T increases H decreases	Weak plunging → Strong plunging
D→A	T = 1.25 s, H = 0.0205 m T = 3.0 s, H = 0.0458 m	[0.0005–0.0019]	T increases H increases	Strong plunging → Surging
A→C diagonal	T = 3.0 s, H = 0.0450 m T = 1.02 s, H = 0.0313 m	[0.0005–0.0055]	T decreases H decreases	Surging → Weak plunging
Transition region	T = 1.75 s, H = 0.10 m T = 2.5 s, H = 0.08 m	[0.0014–0.0040]	T increases H decreases	Weak bore → Strong plunging

CRediT authorship contribution statement

Pilar Díaz-Carrasco: Conceptualization, Funding acquisition, Formal analysis, Data curation, Writing – original draft, Writing – review & editing.

Declaration of competing interest

The authors declare that they have no known competing financial interests or personal relationships that could have appeared to influence the work reported in this paper.

Data availability

Data will be made available on request.

Acknowledgements

The author would like to thank Professor Emeritus Miguel Á. Losada whose help, conceptualisation and earlier draft of the text made this study possible. The first author is funded through the Juan de la Cierva 2020 program (FJC2020-044778-I) by "Unión Europea – NextGenerationEU en el marco del Plan de Recuperación, Transformación y Resiliencia de España", Spanish Ministry of Science and Innovation.

Appendix A. Application of the new experimental technique

Appendix A describes the application of the sample space (Fig. 2) to obtain the wave conditions for the mound breakwaters tested in this study. The design methodology is explained for each slope angle tested in laboratory; that is: (A.1) the sample space for $\cot(\alpha) = 2$; (A.2) the sample space for $\cot(\alpha) = 1.5$.

A.1. Wave conditions for the physical models with slope $\cot(\alpha) = 2$

From the experimental tests performed by Díaz-Carrasco et al. (2020), they concluded that the sample space, $[\log(h/L), \log(H/L)]$, could be a suitable experimental design in laboratory, which: (i) optimises the number of experiments, (ii) verifies the design criteria between model-prototype, and (iii) quantifies the regions of wave energy transformation and the wave breaker types. Then, the sample space elaborated by Díaz-Carrasco et al. (2020), obtained from their tests, was used to design the sample spaces and to select the wave conditions of the experimental tests of this work. Fig. 9 shows the sample space for the physical model tested in Díaz-Carrasco et al. (2020): (RMB) a permeable mound breakwater with a double-layer of cube armour, a porous core (constant B^* and $D_{50,p}$), and a seaward slope angle $\cot(\alpha) = 2$. Based on the sample space shown in Fig. 9, the wave conditions for the physical model with $\cot(\alpha) = 2$ were selected following the flow-chart of Fig. 2 with the following requirements:

- To ensure wave generation in Stokes I regime, the space $[\log(h/L), \log(H/L)]$ was reduced (black solid lines) with respect to the space of the RMB — permeable mound breakwater with main armour layer (blue dash lines):
  - Side A–B represents the limit between cnoidal and Stokes I regimes.
  - Side B–C represents the limit between Stokes II and Stokes I regimes.
- Wave conditions of point A and C mark the limit values of the dissipated region and the reflected region, respectively, assumed for this mound breakwater type and geometry.
- Wave conditions of point B limit the wave height for non-overtopping conditions ($H < 0.14$ m) and Stokes I regime. This maximum wave height also ensures non-damage conditions.
- Wave conditions of point D mark the technical limitations of paddle generation: $H > 0.02$ m and $T > 1$ s.
- Wave conditions selected in the transition region (Fig. 9b) to cover the wave breaker types: strong plunging, strong bore and weak bore.

Table 3 includes in detail the wave conditions of Table 2 for the physical models HP-MB-1 and HP-MB-3, both with slope angle $\cot(\alpha) = 2$. The pattern to increase or decrease T and H and the tendency of the breaker types are indicated to follow each side of the sample space (black lines). The number of tests were (3×38) for the model HP-MB-1 and (3×19) for the model HP-MB-3.

It should be noted that points A and C, which mark the region of maximum reflected wave energy and maximum dissipated wave energy, respectively, are assumed values according to the breakwater type and by known values from studies or real maritime works found in the literature. It is recommended to verify these values with (1) energy calculation formulas (e.g. Zanuttigh and Van der Meer (2008), Díaz-Carrasco et al. (2019a)) or (2) some more experimental tests to verify these limits.

A.2. Wave conditions for the physical model with slope $\cot(\alpha) = 1.5$

As mentioned in Section 2, the slope angle is considered as a plotting parameter of the results. The latter means that relationship between h/L and H/L is ordered by the slope angle of the breakwater. Therefore, regular wave conditions for the HP-MB-2 model with slope $\cot(\alpha) = 1.5$ were programmed keeping constant the wave period, T, of the slope $\cot(\alpha) = 2$ and varying the wave height as,

$$\left[\frac{h}{L}\right]_{1.5} = \left[\frac{h}{L}\right]_{2}$$

$$\frac{H_{1.5}}{L} = \frac{H_2}{L}\left(\frac{1/1.5}{1/2}\right)^2$$

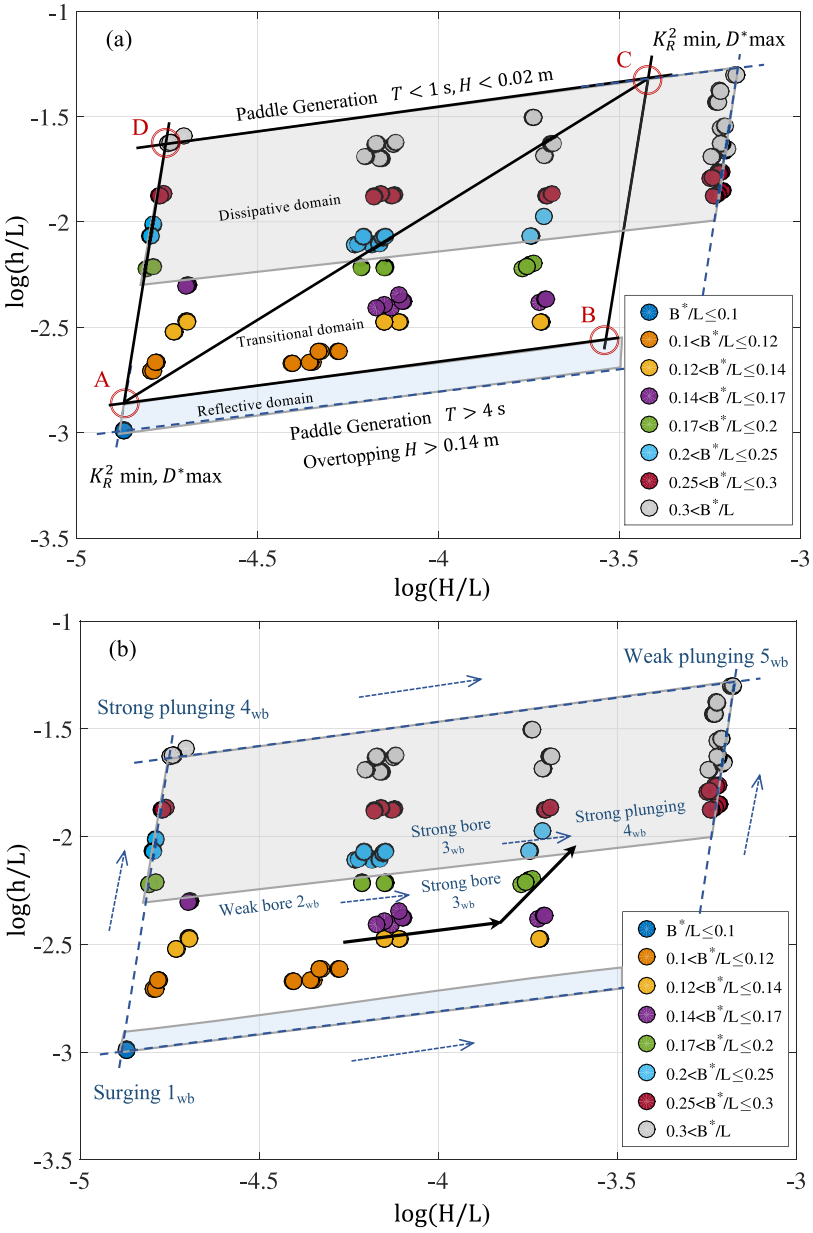

Fig. 9. Sample space $[\log(h/L), \log(H/L)]$ for the homogeneous and permeable mound breakwaters with slope $\cot(\alpha) = 2$ (HP-MB-1 and HP-MB-3). (a) Black solid lines A-B-C-D, regular wave conditions chosen to cover reflected, dissipated and transition regions; (b) black solid arrows, regular wave conditions chosen in the transition region with breaker types strong plunging, strong bore and weak bore. Note that, colours of B^*/L range values and the breaker types are from the experimental results of the permeable mound breakwater with main armour (RMB) tested by Díaz-Carrasco et al. (2020).

Table 4
Regular wave conditions tested for the homogeneous permeable mound breakwater with slope $\cot(\alpha) = 1.5$ (HP-MB-2). (**) wave conditions imposing the same sample space of the slope $\cot(\alpha) = 2$.

Side	Wave conditions	$[(h/L)(H/L)]$	Pattern	Breaker types
A→B	$T = 3$ s, $H = 0.081$ m $T = 2.5$ s, $H = 0.121$ m	[0.0007–0.0022]	T decreases H increases	Weak bore → Strong bore
B→C	$T = 2.5$ s, $H = 0.121$ m $T = 1.02$ s, $H = 0.0556$ m	[0.0022–0.0097]	T decreases H decreases	Strong bore → Weak plunging
C→D	$T = 1.02$ s, $H = 0.0556$ m $T = 1.25$ s, $H = 0.0364$ m	[0.0034–0.0097]	T increases H decreases	Weak plunging → Strong plunging
D→A	$T = 1.25$ s, $H = 0.0364$ m $T = 3$ s, $H = 0.081$ m	[0.0007–0.0034]	T increases H increases	Strong plunging → Strong bore
Transition region	$T = 2.14$ s, $H = 0.12$ m $T = 2.5$ s, $H = 0.08$ m	[0.0014–0.0030]	T increases H decreases	Strong bore → Strong plunging

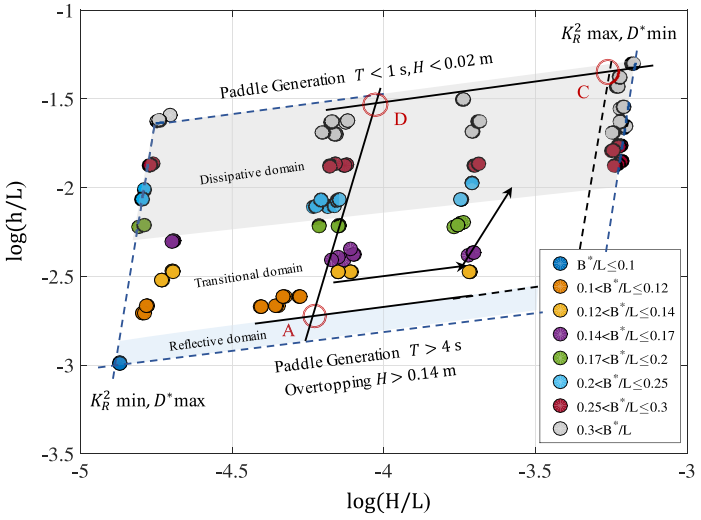

Fig. 10. Sample space $[\log(h/L), \log(H/L)]$ for the homogeneous and permeable mound breakwaters with slope $\cot(\alpha) = 1.5$ (HP-MB-2). Black solid lines A-B-C-D, wave conditions chosen to cover reflected, dissipated and transition regions. Black solid arrows, wave conditions chosen in the transition region with breaker types strong plunging, strong bore and weak bore.

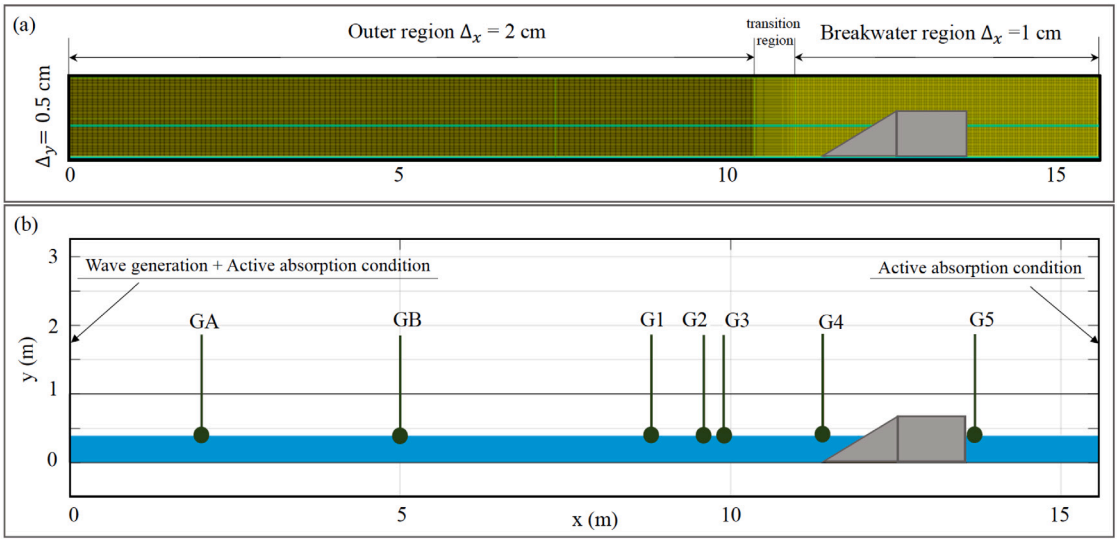

Fig. 11. Numerical domain in IH-2VOF model: (a) mesh grid, (b) wave gauges position.

Table 4 gathers conditions $[H, T]$ selected from the sample space showed in Fig. 10. More wave conditions in the transition region were also selected to cover the breaker types strong plunging, strong bore and weak bore.

Appendix B. Numerical tests using the IH-2VOF model

Model description

The IH-2VOF numerical model (Lara et al., 2008b) was used in Díaz-Carrasco et al. (2020) to model the interaction between waves and an impermeable slope breakwater under non-overtopping conditions. IH-2VOF solves the two-dimensional Reynolds Averaged Navier–Stokes (RANS) equations outside the porous media using the $k - \epsilon$ turbulent model to calculate the kinetic energy (k) and the turbulent dissipation rate (ϵ). The free-surface is tracked by the Volume of Fluid (VOF) method (Hirt and Nichols, 1981). The flow through the porous media is solved by the Volume-Averaged Reynolds Averaged Navier–Stokes (VARANS) equations. The final form of these equations are (more details in Hsu et al. (2002)):

$$\frac{\partial \overline{u_i}}{\partial x_i} \tag{3}$$

$$\frac{1 + c_A}{n_p} + \frac{\overline{u_j}}{n_p^2}\frac{\partial \overline{u_i}}{\partial x_j} = -\frac{1}{\rho_w}\frac{\partial \overline{p}}{\partial x_i} + \frac{\nu}{n_p}\frac{\partial^2 \overline{u_i}}{\partial x_i \partial x_j} - I - \overline{F_{gi}} \tag{4}$$

where t denotes time; u is the Reynolds-averaged velocity; p is the pressure; n_p is the core porosity; ν is the kinematic viscosity; and i, j =1, 2 where 1 and 2 denote the horizontal and vertical directions, respectively. The $\overline{X}$ represents the time-averaged volume-averaged of the variable X. F_{gi} represents the body forces, namely gravity; and I is the hydraulic gradient, which represents the flow resistance forces inside the porous media by the extended Forchheimer equation. The mass added term appears on the left side of the equation, which

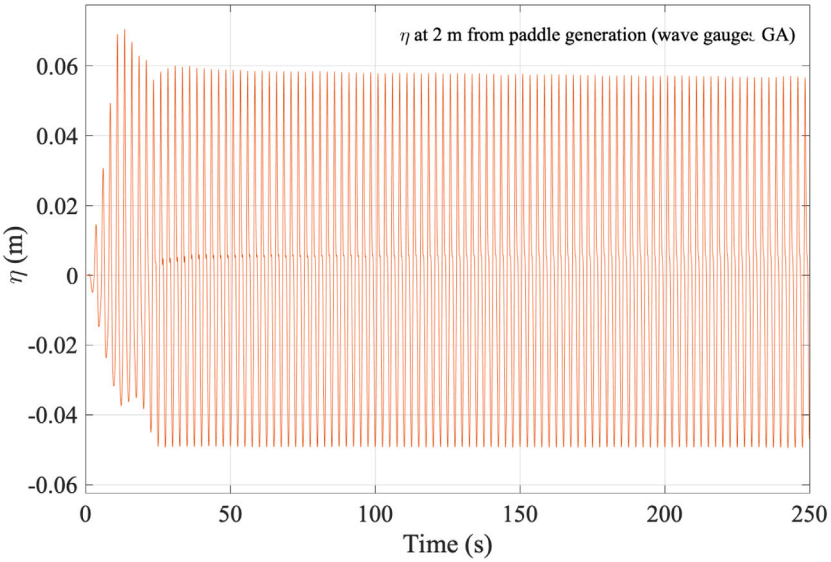

Fig. 12. Free surface, η, measured at 2 m from paddle generation (wave gauge GA) with target wave conditions: H = 0.1059 m and T = 2.5 s.

affects the acceleration term, where $c_A = \gamma_p(1 - n_p)/n_p$ is the added mass coefficient. The value of $\gamma_p = 0.34$ is generally considered to be constant (Van Gent, 1995).

Since the breakwater tested with the numerical model was impermeable, parameters related with the porous media and the flow resistance forces inside the porous media were not taken into account ($n_p = 0$). The reader can find in Vílchez (2016)'thesis an example of calibration of the coefficients involved in the flow inside and outside the porous media for five breakwater typologies.

Numerical setup

A 2D domain of the wave flume described in Fig. 1 was reproduced in the IH-2VOF model. The numerical domain was slightly shorter in the x-direction (15.6 m long) than the wave flume as the dissipation ramp was substituted by an active absorption condition to reduce the number of cells. A uniform mesh on the y-direction was used with a grid cell size of 0.5 cm. The x-direction was divided in 2 subzones as defined in Fig. 11: (1) the 10.4 m-long outer region corresponding to the wave generation zone with a cell size of 2 cm, (2) the region corresponding to the breakwater (wave-structure interaction), where higher accuracy is needed, with a cell size of 1 cm. The total number of cells in the numerical domain was 1017 (x-direction) x 201 (y-direction). A mesh sensitivity analysis was performed to assess the computational cost and the accuracy of the results. Fig. 12 shows the free surface, η, of wave gauge positioned 2 m from the paddle (GA in Fig. 11), for a numerical test characterised by regular wave conditions in paddle: (target) H = 0.1059 m and T = 2.5 s. It is observed that with the mesh size described, the wave measured by GA has the same wave period T = 2.5 s and practically the same wave height H = 0.107 m as the wave conditions imposed to the paddle.

The numerical model was an impermeable slope, $\cot(\alpha) = 2$, over a impermeable caisson. The wave interaction took place only over the impermeable slope. The active wave absorption condition was considered at the generation boundary and at the end of the domain to reproduce the same conditions as in the laboratory. Numerical wave gauges GA and GB measured the free surface away from the structure and were positioned to study the mesh sensitivity. The reflected wave energy, (K_R^2) were obtained by applying power spectral analysis with the data measured by gauges G1, G2 and G3. The transmission coefficient (K_T^2) was computed with the data measured with gauge G5, and for the impermeable and non-overtoppable slope $K_T^5 = 0$. Gauge G4, located at the toe of the structure (x = 0), provided the total wave height at the toe of the breakwater (due to the interaction of the incident and reflected wave trains). The time step was Δ_t = 0.05 s.

Regular waves were simulated by setting $T = [1, 3]$ and varying H to cover the Iribarren domain, $I_r = [2.3, 3.0, 3.5, 4, 4.8, 5]$, with a constant water depth h = 0.4 m (the same as in the physical tests). The minimum number of Iribarren tested was limited by the maximum wave height in non-overtopping conditions. Each test was simulated three time with 100 waves.

References

Ahrens, J.P., 1984. Reef type breakwaters. Coast. Eng. Proc. 1 (19), 178.
Ahrens, J.P., 1989. Stability of reef breakwaters. J. Waterw. Port Coast. Ocean Eng. 115 (2), 221–234.
Baquerizo, A., 1995. Reflexión del oleaje en playas. Métodos de evaluación y de predicción (Ph.D. thesis). University of Cantabria (Spain).
Battjes, J.A., 1974. Surf similarity. In: Proceedings of 14th International Conference on Coastal Engineering. ASCE, pp. 466–480.
Burcharth, H.F., Andersen, O.K., 1995. On the one-dimensional steady and unsteady porous flow equations. Coast. Eng. 24, 233–257.
CIRIA, CUR, CETMEF, 2007. The Rock Manual: The Use of Rock in Hydraulic Engineering. CIRIA, London, p. C683.
Clavero, M., Folgueras, P., Díaz-Carrasco, P., Ortega-Sánchez, M., Losada, M.A., 2018. A similarity parameter for breakwaters: the modified iribarren number. In: Proceedings of 36th International Conference on Coastal Engineering. Baltimore, Maryland (USA).
Dai, Y.B., Kamer, A.M., 1969. Scale effect tests for rubble mound breakwaters. Research Report H-69-2, U. S. Army Engineer Waterway Experiment Station, Corps of Engineers, Vicksburg, Mississippi.
Díaz-Carrasco, P., 2019. Water-wave interaction with mound breakwaters: from the seabed to the armour layer (Ph.D. thesis). University of Granada (Spain).
Díaz-Carrasco, P., Eldrup, M.R., Lykke Andersen, T., 2019a. Wave-breakwater interaction: Test program in the flume of aalborg university. Technical documentation, Department of Civil Engineering, Aalborg University.
Díaz-Carrasco, P., Eldrup, M.R., Lykke Andersen, T., 2021. Advance in wave reflection estimation for rubble mound breakwaters: The importance of the relative water depth. Coast. Eng. 168.
Díaz-Carrasco, P., Moragues, M.V., Clavero, M., Losada, M.A., 2020. 2D water-wave interaction with permeable and impermeable slopes: dimensional analysis and experimental overview. Coast. Eng. 158, 103682.
Gu, Z., Wang, H., 1991. Gravity waves over porous bottom. Coast. Eng. 15, 497–524.
Hirt, C., Nichols, B., 1981. Volume of fluid (VOF) method for dynamics of free boundaries. J. Comput. Phys. 39, 201–225.
Hsu, T., Sakakiyama, T., Liu, P., 2002. A numerical model for wave motions and turbulence flows in front of a composite breakwater. Coast. Eng. 46, 25–50.
Iribarren, C.R., Nogales, C., 1949. Protection des ports. In: Paper presented at 17th International Navigation Congress, Permanent Int. Association of Navigation Congress, Lisbon (Portugal.
Kortenhaus, A., Oumeraci, H., 1998. Classification of wave loading on monolithic coastal structures. Coast. Eng. 26, 867–880.

Lakehal, D., Liovic, P., 2011. Turbulence structure and interaction with steep breaking waves. J. Fluid Mech. 674, 522–577.
Lara, J.L., Losada, I.J., Guanche, R., 2008a. Wave interaction with low-mound breakwaters using a RANS model. Ocean Eng. 35 (13), 1388–1400.
Lara, J.L., Losada, I.J., Guanche, R., 2008b. Wave interaction with low-mound breakwaters using a RANS model. Ocean Eng. 35, 1388–1400.
Losada, M.A., 2021. Method to assess the interplay of slope, relative water depth, wave steepness, and sea state persistence in the progression of damage to the rock layer over impermeable dikes. Ocean Eng. 239, 109904.
Molines, J., Centi, R., Di Risio, M., Medina, J.R., 2021. Estimation of layer coefficients of cubipod homogeneous low-crested structures using physical and numerical model placement tests. Coast. Eng. 168, 103901.
Moragues, M.V., Losada, M.A., 2021. Progression of wave breaker types on a plane impermeable slope, depending on experimental design. J. Geophys. Res.: Ocean 126, 5.
Odériz, I., Mendoza, E., Silva, R., Medina, J.R., 2018. Stability and hydraulic performance of a homogeneous cubipod low-crested mound breakwater. In: Proceedings of the 7th International Conference on the Application of Physical Modelling in Coastal and Port Engineering and Science (Coastlab18).
Pérez-Romero, D.M., Ortega-Sánchez, M., Moñino, A., Losada, M.A., 2009. Characteristic friction coefficent and scale effects in oscillatory flow. Coast. Eng. 56, 931–939.
Requejo, S., Vidal, C., Losada, I.J., 2002. Modeling of wave loads and hydraulic performance of vertical permeable structures. Coast. Eng. 46, 249–276.
Scarcella, D., Benedicto, M., Moñino, A., Losada, M.A., 2007. Scale effects in rubble mound breakwaters considering wave energy balance. In: Proceedings of the 30th Coastal Engineering Conference. pp. 4410–4416.
Van Gelder, P., 2001. Statistical methods for the risk-based design of civil structures.
Van Gent, M.R., 1995. Wave Interaction with Permeable Coastal Structures (Ph.D. thesis). Delft University.
Vílchez, M., 2016. An unified design method of maritime works against waves (Ph.D. thesis). University of Granada (Spain).
Vílchez, M., Clavero, M., Lara, J., Losada, M.A., 2016. A characteristic friction diagram for the numerical quantification of the hydraulic performance of different breakwater types. Coast. Eng. 114, 86–98.
Zanuttigh, B., Van der Meer, J.W., 2008. Wave reflection from coastal structures in design conditions. Coast. Eng. 55, 771–779.
Zhang, Q., Liu, P., 2008. A numerical study of swash flows generated by bores. Coast. Eng. 55, 1113–1134.